Inorganic Chemistry

pubs.acs.org/IC

Article

Photochemistry and Photophysics of Charge-Transfer Excited States in Emissive d^{10}/d^0 Heterobimetallic Titanocene Tweezer Complexes

Henry C. London, David Y. Pritchett, Jared A. Pienkos, Colin D. McMillen, Thomas J. Whittemore, Conor J. Bready, Alexis R. Myers, Noah C. Vieira, Shannon Harold, George C. Shields,* and Paul S. Wagenknecht*

Cite This: *Inorg. Chem.* 2022, 61, 10986–10998

Read Online

ACCESS | Metrics & More | Article Recommendations | Supporting Information

ABSTRACT: Transition-metal complexes that undergo ligand-to-metal charge transfer (LMCT) to d^0 metals are of interest as possible photocatalysts due to the lack of deactivating d−d states. Herein, the synthesis and characterization of nine titanocene complexes of the formula $Cp_2Ti(C_2Ar)_2{\cdot}MX$ (where Ar = phenyl, dimethylaniline, or triphenylamine; and MX = CuCl, CuBr, or AgCl) are presented. Solid-state structural characterization demonstrates that MX coordinates to the alkyne tweezers and CuX coordination has a greater structural impact than AgCl. All complexes, including the parent complexes without coordinated MX, are brightly emissive at 77 K (emission max between 575 and 767 nm), with the coordination of MX redshifting the emission in all cases except for the coordination of AgCl into $Cp_2Ti(C_2Ph)_2$. TDDFT investigations suggest that emission is dominated by arylalkynyl-to-titanium ^{3}LMCT in all cases except $Cp_2Ti(C_2Ph)_2{\cdot}CuBr$, which is dominated by CuBr-to-Ti charge transfer. In room-temperature fluid solution, only $Cp_2Ti(C_2Ph)_2$ and $Cp_2Ti(C_2Ph)_2{\cdot}AgCl$ are emissive, albeit with photoluminescent quantum yields $\leq 2 \times 10^{-4}$. The parent complexes photodecompose in room-temperature solution with quantum yields, Φ_{rxn}, between 0.25 and 0.99. The coordination of MX decreases Φ_{rxn} by two to three orders of magnitude. There is a clear trend that Φ_{rxn} increases as the emission energy increases. This trend is consistent with a competition between energy-gap-law controlled nonradiative decay and thermally activated intersystem crossing between the ^{3}LMCT state and the singlet transition state for decomposition.

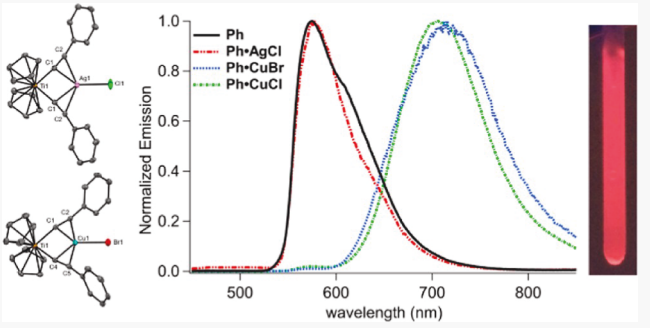

INTRODUCTION

Transition-metal complexes with long-lived excited states have played a central role in photocatalysis,[1,2] phosphorescent complexes for use in organic light-emitting diodes (OLEDs),[3−5] and biological sensors.[6,7] Complexes of Ru, Ir, and Pt have dominated these applications, but these metals are expensive and relatively rare. Thus, recent investigations have focused on replacing these metals with earth-abundant materials.[8−28] For example, complexes of earth-abundant second- and third-row transition metals (e.g., Mo and W) have been investigated as possible photocatalysts.[9−12] Complexes of first-row transition metals, on the other hand, suffer from thermal accessibility of metal-centered (MC) states due to these states being at lower energies than their second- and third-row counterparts. These MC states are known to undergo rapid, nonradiative deactivation, sometimes leading to decomposition. Therefore, their accessibility serves as a nonradiative sink.[29] Destabilizing the MC states through the use of high-field ligands is a common strategy to overcome this limitation. For example, complexes of Cr^0 and Mn^I, where high-field, chelating isocyanide ligands have been utilized to destabilize the ^{3}MC states, are emissive in room-temperature (RT) fluid solution.[17] Likewise, a facial tris-carbene ligand that provides improved orthoaxial coordination around Fe^{III} suppresses deactivation through the MC states, resulting in an Fe^{III} complex that is also emissive in RT fluid solution.[18] Another strategy has taken advantage of long-lived, emissive, intraconfigurational MC excited states in complexes of Cr^{III}.[19−21] Yet another approach eliminates MC states, altogether, by using complexes of transition metals having a d^{10} electronic configuration, chiefly Cu^I.[22−26] More recently, this strategy of eliminating MC states has focused on ligand-to-metal charge-transfer (LMCT) excited states in complexes of d^0 metals, chiefly Zr^{IV}.[30−33]

The earliest examples of emissive d^0 complexes involve LMCT states of simple metallocenes of Sc^{III},[34] Ti^{IV},[35,36] and Zr^{IV} (Figure 1).[37,38] Both the scandocene and zirconocene

Received: May 20, 2022
Published: July 4, 2022

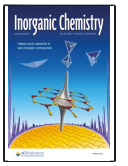

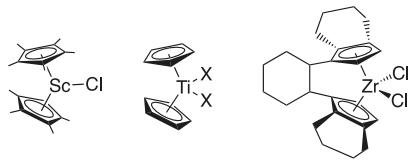

Figure 1. Emissive metallocene complexes of d^0 metals.

complexes are emissive in RT fluid solution, whereas emission from the titanocenes is only reported in 77 K glass. More recently, a Zr^{IV} pyridine dipyrrolide complex has been shown to be emissive in RT fluid solution and has been shown to be a photoredox catalyst as well as a photosensitizer for triplet−triplet annihilation-based photon upconversion.[30−32] Furthermore, the very simple and commercially available titanocene, Cp_2TiCl_2, has recently been demonstrated to act as a photoredox catalyst for epoxide reduction.[39,40] These cases suggest that with the proper design considerations, long-lived emissive excited states involving LMCT transitions in d^0 complexes of first−row transition metals (e.g., Ti and Sc) should be possible, and such complexes may serve as photoredox catalysts.

In an effort to rationally design d^0 metallocene-based photoredox catalysts, our group recently began an investigation of the photophysics and photochemistry of a series of arylalkynyltitanocenes, $Cp_2Ti(C_2R)_2$ (Figure 2).[41,42] In 77 K

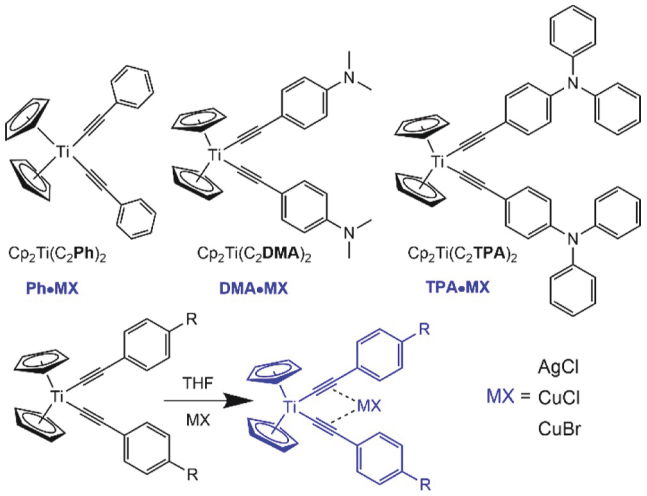

Figure 2. Top: Arylalkynyltitanocenes previously investigated. The abbreviations for each complex indicate the substituent on the alkynyl ligand (**Ph** = phenyl, **DMA** = dimethylaniline, and **TPA** = triphenylamine). Bottom: Synthesis of the corresponding heterobimetallic tweezer complexes, **Ph·MX**, **DMA·MX**, and **TPA·MX**.

solvent glass, these complexes are highly emissive from an arylethynyl-to-titanium ^{3}LMCT state. The emission is tunable between 575 and 672 nm, depending on the arylethynyl ligand. In RT fluid solution, the complexes undergo photodecomposition with quantum yields between 0.25 and 0.99, hampering consideration as photocatalysts. In an earlier investigation, we reported that the coordination of CuBr into the alkyne tweezers of Cp_2*$Ti(C_2$2-py$)_2$ (where Cp* = pentamethylcyclopentadienyl and $C_2$2-py = 2-ethynylpyridine) resulted in a complex that was stable under ambient light.[43] No further analysis was performed. Herein, we investigate the impact that the coordination of CuCl, CuBr, or AgCl in the alkyne tweezers (Figure 2) has on the photochemistry and photophysics of the coordinated titanocenes. Such d^{10}/d^0 systems provide the opportunity for metal halide-to-metal charge transfer (MXMCT), but without the interference of ^{3}MC states. Our chief findings are that all complexes are highly emissive in 77 K solvent glass and the coordination of MX lowers the excited-state energies. For most complexes, the lowest-energy excited states are of LMCT character. One exception is **Ph·CuBr**, for which the lowest-energy triplet is dominated by MXMCT from CuBr to Ti^{IV}. The stability of the complexes toward photodecomposition decreases as the excited-state energy increases. This trend is consistent with a model where thermally activated intersystem crossing from the emissive ^{3}CT state to the reactive transition state is in competition with nonradiative decay controlled by the energy-gap law. Lastly, two of the complexes, $Cp_2Ti(C_2Ph)_2$ and **Ph·AgCl**, are weakly emissive in room-temperature fluid solution. To our knowledge, these are the first examples of emission from complexes of Ti^{IV} in room-temperature fluid solution.

EXPERIMENTAL SECTION

Materials and Methods. The complexes $Cp_2Ti(C_2Ph)_2$, $Cp_2Ti(C_2DMA)_2$, and $Cp_2Ti(C_2TPA)_2$ were prepared according to literature procedures.[41] All reactions were carried out under air-free conditions using standard Schlenk techniques. Tetrahydrofuran (THF) was dried and degassed using an Innovative Technologies solvent purification system before use. NMR spectra were obtained using a Varian 400-MR or INOVA-500 spectrometer. Infrared spectra were obtained using a PerkinElmer Spectrum Two FT-IR spectrometer with a UATR attachment. UV−vis absorption spectra were recorded using a Cary-50 spectrophotometer with the cell holder thermostated to 20 °C using a Quantum Northwest TLC-50 cuvet holder. Emission spectra were recorded using a HORIBA Fluorolog-3 Spectrofluorimeter equipped with either an FL-1013 liquid nitrogen dewar assembly or a J-1933 solid-sample holder. Relative solution-state photoluminescence quantum yield for $Cp_2Ti(C_2Ph)_2$ was determined from the ratio of the slope of plots of integrated emission intensity versus absorbance for the analyte versus a quinine sulfate standard. Emission lifetimes were measured using a Photon Technology International (PTI) GL-3300 pulsed nitrogen laser fed into a PTI GL-302 dye laser as the excitation source. The resulting data set was collected on an OLIS SM-45 EM fluorescence lifetime measurement system using a Hamamatsu R928 photomultiplier tube fed through a variable feed-through terminator into a LeCroy Wavejet 352A oscilloscope and analyzed using OLIS Spectral Works. Elemental analyses were performed by Midwest Microlabs.

Syntheses. *General Method.* To an oven-dried, two-neck round-bottom flask (50 mL) under a positive pressure of argon and protected from light was added 100 mg of the desired titanocene, the appropriate metal−halide (1 to 4 equiv), and THF (10 mL). This solution was stirred for 2 to 6 h. The remaining steps were performed under air. The solvent was removed from the reaction by rotary evaporation. The solid was then loaded onto a silica gel column (2.5 × 12 cm) and eluted with 5% triethylamine in CH_2Cl_2. The deeply colored band was collected, and the solvent was removed by rotary evaporation. The resulting solid was dissolved in minimal CH_2Cl_2 (2 mL) and precipitated with hexanes (20 mL). The precipitate was collected using vacuum filtration, washed with Et_2O (2 mL), and dried under vacuum.

*$Cp_2Ti(C_2Ph)_2$CuBr (**Ph·CuBr**).* Using $Cp_2Ti(C_2Ph)_2$ (100 mg, 0.263 mmol), CuBr (95.6 mg, 0.666 mmol, 2.5 equiv), and a reaction time of 2 h resulted in 85 mg (62%) of a bright orange solid. UV−vis (CH_2Cl_2), λ/nm (ε/dm^3 mol^{-1} cm^{-1}): 489 (5040), 393 (10000). UV−vis (THF), λ/nm (ε/dm^3 mol^{-1} cm^{-1}): 492 (3950), 401 (8890). ^{1}H NMR (400 MHz, $CDCl_3$): δ 7.64 (d, 4H), 7.36 (m, 6H), 6.12 (s, 10H). ^{13}C NMR (400 MHz, $CDCl_3$): δ 144.72, 138.95, 132.58, 129.20, 128.26, 123.56, 110.69. Anal. calc (found) for $C_{26}H_{20}TiCuBr$,

https://doi.org/10.1021/acs.inorgchem.2c01746
Inorg. Chem. 2022, 61, 10986−10998

C, 59.62 (60.13), H, 3.85 (3.98). IR (neat) ν(C≡C) = 2000, 1968 cm^{-1}.

*$Cp_2Ti(C_2DMA)_2CuBr$ (**DMA·CuBr**).* Using $Cp_2Ti(C_2DMA)_2$ (100 mg, 0.214 mmol), CuBr (61.5 mg, 0.428 mmol, 2 equiv) and a reaction time of 2 h resulted in 114 mg (87%) of a black solid. UV−vis (CH_2Cl_2), λ/nm (ε/dm^3 mol^{-1} cm^{-1}): 584 (15,350), 400 (17,800). UV−vis (THF), λ/nm (ε/dm^3 mol^{-1} cm^{-1}): 571 (9,910), 390 (16,900). ^{1}H NMR (400 MHz, $CDCl_3$): δ 7.44 (d, J = 9.1 Hz, 4H), 6.65 (d, J = 9.1 Hz, 4H), 6.06 (s, 10H), 2.99 (s, 12H). ^{13}C NMR (400 MHz, $CDCl_3$): δ 150.73, 144.32, 143.21, 133.95, 111.65, 109.78, 109.41, 40.13. Anal. calcd (found) for $C_{30}H_{30}N_2TiCuBr$, C, 59.08(59.13); H, 4.96 (5.05); N, 4.59 (4.52). IR (neat) ν(C≡C) = 1959 cm^{-1}.

*$Cp_2Ti(C_2TPA)_2CuBr$ (**TPA·CuBr**).* Using $Cp_2Ti(C_2TPA)_2$ (100 mg, 0.140 mmol), CuBr (40.1 mg, 0.280 mmol, 2 equiv), and a reaction time of 2 h resulted in 94 mg (78%) of a black solid. UV−vis (CH_2Cl_2), λ/nm (ε/dm^3 mol^{-1} cm^{-1}): 563 (13,700), 400 (16,800). UV−vis (THF), λ/nm (ε/dm^3 mol^{-1} cm^{-1}): 550 (10,700), 402 (15,100). ^{1}H NMR (500 MHz, $CDCl_3$) δ7.45 (d, J = 8.8 Hz, 4H), 7.26 (m, 8H), 7.12 (d, 8H), 7.06 (m, 4H), 6.99 (d, J = 8.8 Hz, 4H), 6.08 (s, 10H). ^{13}C NMR (500 MHz, $CDCl_3$): δ 148.71, 147.22, 144.80, 140.89, 133.69, 129.51, 125.39, 123.80, 121.79, 115.67, 110.33. Anal. calcd (found) for $C_{50}H_{38}N_2TiCuBr$, C, 69.98(69.90); H, 4.46(4.59); N, 3.26(3.26). IR (neat) ν(C≡C) = 1973, 1961 cm^{-1}.

*$Cp_2Ti(C_2Ph)_2CuCl$ (**Ph·CuCl**).* Using $Cp_2Ti(C_2Ph)_2$ (100 mg, 0.263 mmol), CuCl (95.6 mg, 0.965 mmol, 4 equiv), and a reaction time of 3 h resulted in 85.1 mg (65%) of a red orange solid. UV−vis (CH_2Cl_2), λ/nm (ε/dm^3 mol^{-1} cm^{-1}): 484 (4588), 373 (8,485). UV−vis (THF), λ/nm (ε/dm^3 mol^{-1} cm^{-1}): 486 (3920), 389 (8054). ^{1}H NMR (400 MHz, $CDCl_3$): δ 7.65 (d, J = 2.4 Hz, 4H), 7.36 (m, 6H), 6.11 (s, 10H). ^{13}C NMR (400 MHz, $CDCl_3$): δ 143.91, 138.57, 132.13, 128.92, 128.16, 123.11, 110.39. Anal. calc (found) for $C_{26}H_{20}TiCuCl$, C, 65.15 (64.75); H, 4.21 (4.51). IR (neat) ν(C≡C) = 1967, 1998 cm^{-1}.

*$Cp_2Ti(C_2DMA)_2CuCl$ (**DMA·CuCl**).* Using $Cp_2Ti(C_2DMA)_2$ (100 mg, 0.214 mmol), CuCl (90 mg, 0.866 mmol, 4 equiv), and a reaction time of 3 h resulted in 107 mg (88%) of a dark blue solid. UV−vis (CH_2Cl_2), λ/nm (ε/dm^3 mol^{-1} cm^{-1}): 570 (13,600), 397 (16,900). UV−is (THF), λ/nm (ε/dm^3 mol^{-1} cm^{-1}): 570 (10,000), 392 (16,700). ^{1}H NMR (400 MHz, $CDCl_3$): δ 7.45 (d, J = 9.1 Hz, 4H), 6.64 (d, J = 9.1 Hz, 4H), 6.04 (s, 10H), 2.98 (s, 10H). ^{13}C NMR (500 MHz, $CDCl_3$): δ 150.67, 143.58, 142.54, 133.69, 111.72, 109.70, 109.28, 40.17. Anal. calc (found) for $C_{30}H_{30}N_2TiCuCl$, C, 63.72 (63.35); H, 5.35 (5.64); N, 4.95 (4.93). IR (neat) ν(C≡C) = 1960 cm^{-1}.

*$Cp_2Ti(C_2TPA)_2CuCl$ (**TPA·CuCl**).* Using $Cp_2Ti(C_2TPA)_2$ (100 mg, 0.140 mmol), CuCl (55 mg, 0.56 mmol, 4 equiv), and a reaction time of 3 h resulted in 51.3 mg (45%) of a dark blue solid. UV−vis (CH_2Cl_2), λ/nm (ε/dm^3 mol^{-1} cm^{-1}): 556 (12,200), 400 (16,200). UV−vis (THF), λ/nm (ε/dm^3 mol^{-1} cm^{-1}): 544 (8910), 395 (15,800). ^{1}H NMR (400 MHz, $CDCl_3$): δ 7.46 (d, J = 9.0 Hz, 4H), 7.25 (m, 8H), 7.11 (d, J = 8.6 Hz, 12H), 7.05 (m, 4H), 6.99 (d, J = 8.9 Hz, 4H), 6.07 (s, 10H). ^{13}C NMR (400 MHz, $CDCl_3$): δ 148.46, 147.08, 140.15, 133.30, 129.39, 125.15, 125.03, 123.58, 121.81, 115.39, 110.08. Anal. calc (found) for $C_{50}H_{38}N_2TiCuCl{\cdot}1.5H_2O$: C, 71.43 (71.46); H, 4.92 (4.63); N, 3.33 (3.77). IR (neat) ν(C≡C) = 1982, 1968 cm^{-1}.

*$Cp_2Ti(C_2Ph)_2AgCl$ (**Ph·AgCl**).* Using $Cp_2Ti(C_2Ph)_2$ (100 mg, 0.241 mmol), AgCl (34.6 mg, 0.241 mmol, 1 equiv), and a reaction time of 6 h resulted in 59.2 mg (43%) of an orange solid. UV−vis (CH_2Cl_2), λ/nm (ε/dm^3 mol^{-1} cm^{-1}): 417 (9700), 313 (18,200). UV/Vis (THF), λ/nm (ε/dm^3 mol^{-1} cm^{-1}): 414 (7170), 313 (13,900). 1 H NMR (400 MHz, $CDCl_3$): δ 7.64 (d, J = 7.2 Hz, 4H), 7.36 (m, 6H), 6.30 (s, 10H). Anal. calcd (found) for $C_{26}H_{20}AgClTi$, C, 59.64 (59.93); H, 3.85 (4.03). IR (neat) ν(C≡C) = 2024, 1979 cm^{-1}.

*$Cp_2Ti(C_2DMA)_2AgCl$ (**DMA·AgCl**).* Using $Cp_2Ti(C_2DMA)_2$ (100 mg, 0.214 mmol), AgCl (30.7 mg, 0.214 mmol, 1 equiv), and a reaction time of 6 h resulted in 26.1 mg (20.0%) of a dark blue solid. UV−vis (CH_2Cl_2), λ/nm (ε/dm^3 mol^{-1} cm^{-1}): 590 (19,100), 445 (5160). UV−vis (THF), λ/nm (ε/dm^3 mol^{-1} cm^{-1}): 581 (16,300), 428 (6315). ^{1}H NMR (400 MHz, $CDCl_3$): δ 7.41 (d, J = 8.5 Hz, 4H), 6.63 (d, J = 8.5 Hz, 4H), 6.22 (s, 10H), 2.99 (s, 12H). ^{13}C NMR (400 MHz, $CDCl_3$): δ 150.83, 147.46, 134.24, 133.54, 111.86, 111.48, 107.83, 40.14. Anal. calcd (found) for $C_{30}H_3N_2TiAgCl$, C, 58.23 (58.03); H, 5.05 (4.97); N, 4.53 (4.56). IR (neat) ν(C≡C) = 2036, 1999 cm^{-1}.

*$Cp_2Ti(C_2TPA)_2AgCl$ (**TPA·AgCl**).* Using $Cp_2Ti(C_2TPA)_2$ (100 mg, 0.140 mmol), AgCl (20 mg, 0.140 mmol, 1 equiv), and a reaction time of 6 h resulted in 88.2 mg (73%) of a dark purple blue solid. UV−vis (CH_2Cl_2), λ/nm (ε/dm^3 mol^{-1} cm^{-1}): 577 (19,500), 311 (43,600). UV−vis (THF), λ/nm (ε/dm^3 mol^{-1} cm^{-1}): 547 (12,200), 311 (47,800). ^{1}H NMR (400 MHz, $CDCl_3$): δ 7.41 (d, J = 8.7 Hz, 4H), 7.25 (m, 8H), 7.12 (d, J = 7.3 Hz, 8H), 7.06 (m, 4H), 6.97 (d, J = 8.7 Hz, 4H), 6.25 (s, 10H). ^{13}C NMR (400 MHz, $CDCl_3$): δ 148.74, 146.91, 133.38, 132.91, 129.44, 129.39, 125.31, 123.80, 121.66, 121.51, 112.00. Anal. calcd (found) for $C_{50}H_{38}N_2TiAgCl$, C, 4.46(4.56); H, 69.99(70.01); N, 3.27(3.34). IR (neat) ν(C≡C) = 1997, 2019 cm^{-1}.

Photodecomposition Quantum Yields. Quantum yields for complexes with Φ_{rxn} > 0.1 were determined using a focused beam from a Xe short-arc lamp fed through a monochromator according to previously reported procedures (estimated error for Φ_{rxn} = ±20%).[42] The remainder were irradiated at the selected wavelengths using a Rayonet RPR-100 Photochemical Reactor using eight bulbs of either 575 nm (RPR-5750) or 419 nm (RPR-4190), depending on the wavelength of absorption. The contents of the cuvette were stirred continuously during the period of the photolysis. Photon flux for the 419 nm bulbs (1.6×10^{-7} mol/s) was determined using ferrioxalate actinometry.[44] Photon flux for the 575 nm bulbs (1.1×10^{-7} mol/s) was determined using $Cp_2Ti(C_2DMA)_2$ as a chemical actinometer which has a quantum yield for photodecomposition in THF of 0.25.[42] Photon flux measurements were performed with the same sample volume (3 mL) and cell geometry used for the photolyses. All photolyses for quantum yield determinations were performed in THF with 1% triethylamine added to inhibit acid hydrolysis. Initial concentrations were chosen to have an absorbance near 1.5 at the irradiation wavelength and photolysis time was typically chosen to result in a decrease in absorbance of approximately 0.2 absorbance units, ensuring that the fraction of incident radiation absorbed is nearly constant over the course of the photolysis. UV−vis spectra were recorded at 20.0 °C before and after photolysis. Concentration changes were determined by measuring the absorbance change at the LMCT absorbance maximum. All reported Φ_{rxn} are averages of at least three replicates. Estimated error for Φ_{rxn} = ±30%.

Computational Methods. Gaussian 16[45] was used for all DFT and TDDFT calculations. For each computational model, the geometry was optimized and the structure was checked to be a minimum based on the frequency calculation. GaussView, version 6.32[46] was used for all orbital imaging. GaussSum3[47] was used for Mulliken population analysis. Computational models used the functionals B3LYP,[48] MN15,[49] and ωB97XD[50] and the basis sets 6-311+G(d),[51] DGDZVP,[52] and LANL2DZ.[53] ORCA 4.2.1[54] DLPNO-CCSD(T)/cc-pVnZ[55,56] single point calculations (n = D, T, Q) on ωB97XD geometries were used to estimate the CCSD(T) Complete Basis Set (CBS) Gibbs free energy of activation[57,58] for the transition state leading to decomposition of $Cp_2Ti(C_2Ph)_2$.

X-Ray Diffraction. Single crystals of **Ph·AgCl**, **Ph·CuCl**, and **TPA·CuBr** were grown by slow evaporation from a solution of the complex in THF with 5% triethylamine (TEA). Single crystals of **Ph·CuBr** and **DMA·CuBr** were grown by vapor diffusion of Et_2O into a solution of the complex in THF with 5% TEA. Single-crystal X-ray diffraction data were collected at 100 K using a Bruker D8 VENTURE diffractometer with Mo Kα radiation (λ = 0.71073 Å) and a Photon 2 detector. Data collection, data processing (SAINT), scaling, and absorption correction (SADABS, multiscan) were performed using the Apex 3 software suite.[59] Space group determination (XPREP), structure solution by intrinsic phasing (SHELXT), and structure refinement by full-matrix least-squares techniques on F^2 (SHELXL) were performed using the SHELXTL software package.[60] All nonhydrogen atoms were refined anisotropically. Hydrogen atoms

https://doi.org/10.1021/acs.inorgchem.2c01746
Inorg. Chem. 2022, 61, 10986−10998

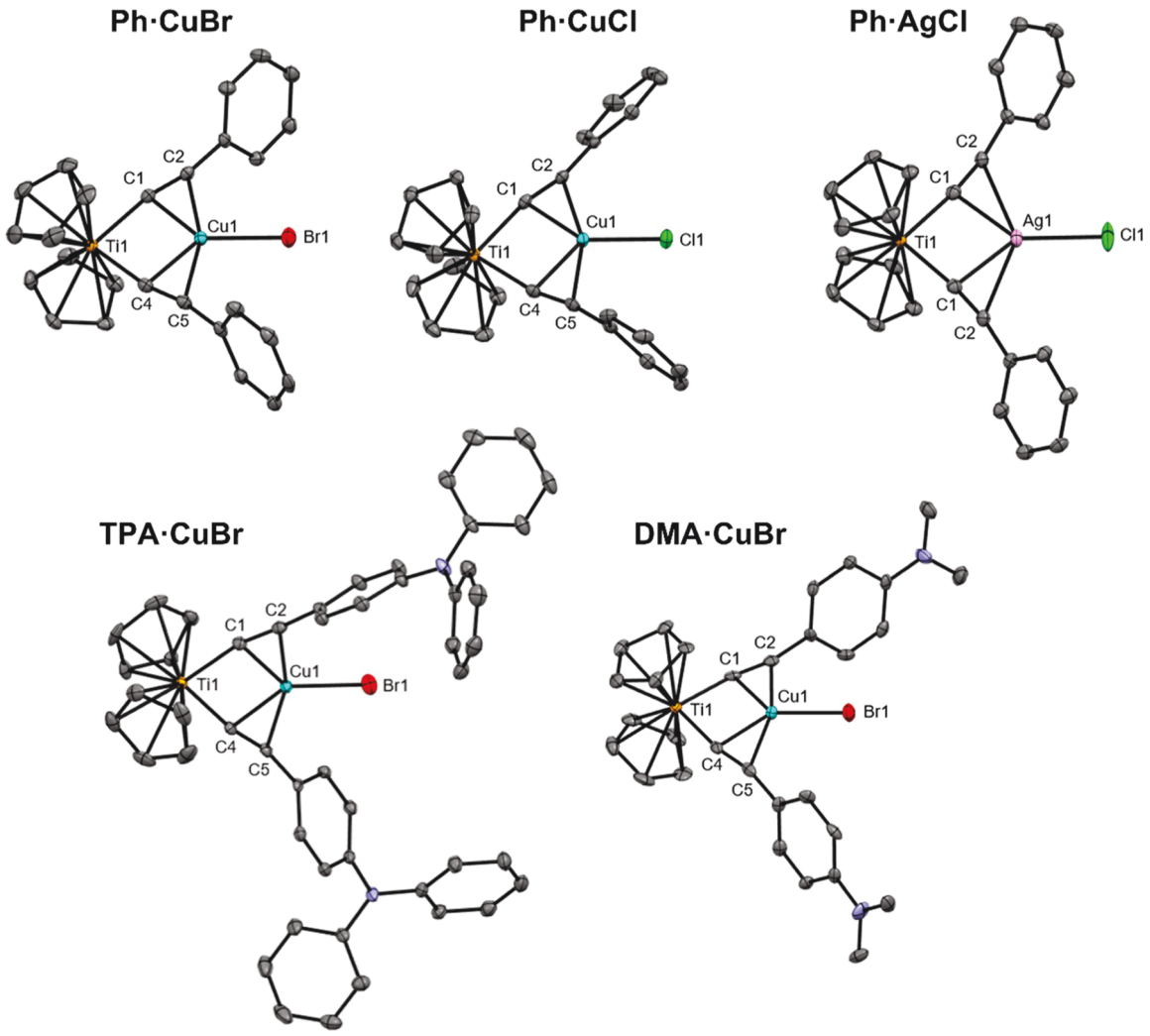

Figure 3. Crystal structures of titanocenes discussed herein: Hydrogen atoms omitted for clarity. Ellipsoids are shown at the 50% probability level.

Table 1. Averaged Geometric Parameters for Titanocenes With and Without Coordinated MX[a,b]

	Ti−C_{alkyne}	C≡C	C−Ti−C	Ti−C≡C	C≡C−C	M−C_1	M−C_2
$Cp_2Ti(C_2Ph)_2$	2.102	1.222	100.68(12)[c]	174.2	177.6		
Ph·AgCl	2.107(2)[c]	1.232(3)[c]	97.53(11)[c]	172.07(17)[c]	171.2(2)[c]	2.278(2)[c]	2.708(2)[c]
Ph·CuCl	2.087	1.231	91.47(8)[c]	168.43	164.65	2.058	2.234
Ph·CuBr[d]	2.097	1.232	90.46	168.02	164.88	2.065	2.211
$Cp_2Ti(C_2DMA)_2$[d]	2.094	1.223	95.25	177.95	177.25		
DMA·CuBr	2.092	1.245	92.7(2)[c]	165.8	167.0	2.067	2.223
TPA·CuBr	2.095	1.234	92.05(11)[c]	167.0	165.7	2.063	2.22

[a]All bond lengths are in Å and angles, in degrees. [b]See Figure 2 for complex abbreviations. [c]There is only one unique value for the bond length or angle, so the uncertainty in the last digit of the crystal structure is reported. [d]Parameters for structures having multiple unique complexes in the asymmetric unit consider all of the unique complexes in the average values.

attached to carbon atoms were placed in calculated positions using appropriate riding models. The structure of **TPA·CuBr** was found to be the THF solvate of the complex, with the THF molecule disordered over two orientations. Crystallographic data are provided in the Supporting Information, Table S1. Crystallographic data are available in CIF form through the Cambridge Crystallographic Data Centre, CCDC deposition numbers 2172550-2172554.

Photochemical Decomposition of Ph·CuBr. A sample of the complex (30 mg) in anhydrous THF (10 mL) was degassed with three freeze−pump−thaw cycles and then irradiated using a Rayonet RPR-100 Photochemical Reactor equipped with eight RPR-4190 bulbs. Organic products were purified by column chromatography (SiO_2, CH_2Cl_2).

RESULTS AND DISCUSSION

Syntheses. Coordination of metal halides (MX = CuBr, CuCl, and AgCl) into the alkyne tweezers of the $Cp_2Ti(C_2R)_2$ complexes followed the precedent of the Lang group (Figure 2),[61−63] wherein the appropriate titanocene is stirred with MX in THF for 2 to 6 h. Due to the low solubility of the metal halides in THF, fine powders of MX resulted in faster reactions than pellets. Due to the oxygen sensitivity of Cu^I salts, all

https://doi.org/10.1021/acs.inorgchem.2c01746
Inorg. Chem. 2022, 61, 10986−10998

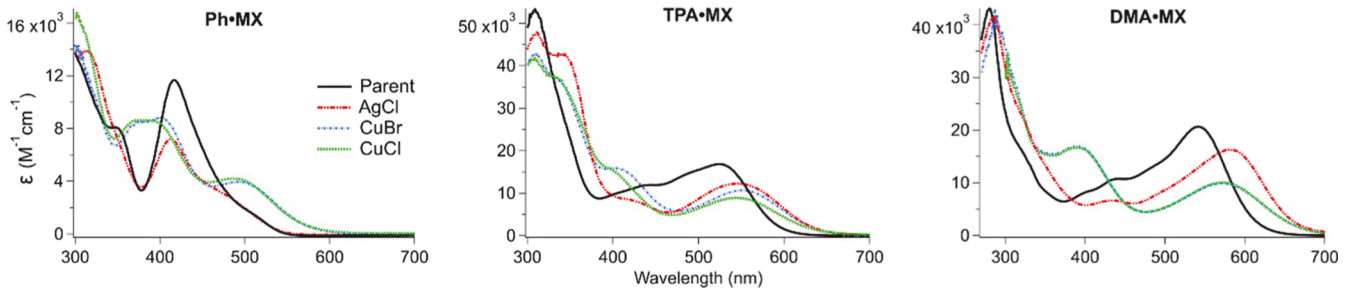

Figure 4. UV−vis absorption spectra in THF at 20 °C.

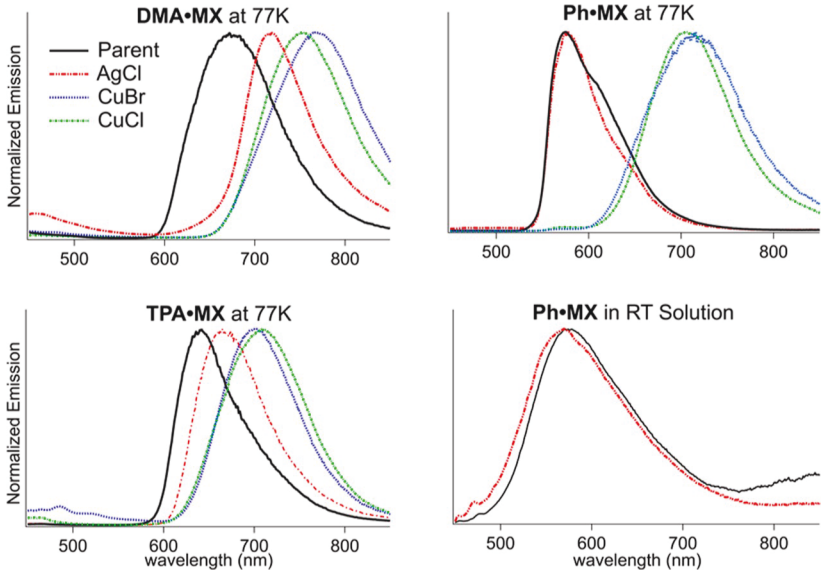

Figure 5. Normalized emission spectra of **DMA·MX** (top left), **Ph·MX** (top right), and **TPA·MX** (bottom left) at 77 K (2-MeTHF) and **Ph·MX** in RT THF solution (bottom right). λ_{ex} = 400 nm. Emission spectra in solution are stirred to moderate the impact of photodecomposition on the spectrum.

reactions were performed under an inert atmosphere. However, both the parent complexes (i.e., the complexes without coordinated MX) and the complexes with coordinated MX are air-stable and can be handled on the benchtop either as solids or in solution. The complexes were purified by column chromatography using 5% triethylamine in dichloromethane. The equilibrium constant for MX coordination is apparently large enough to offset the low solubility of MX and to maintain coordination of MX during column purification.

All MX coordinated complexes were characterized by ^{1}H and ^{13}C NMR spectroscopy, elemental analysis, UV−vis spectroscopy, emission spectroscopy, and IR spectroscopy, and a subset was characterized by X-ray diffraction. The complexes are soluble in THF, CH_2Cl_2, chloroform, benzene, and DMSO but insoluble in ether, hexanes, and methanol. Alkynyltitanocenes are sensitive to acid hydrolysis in solution;[64] long-term stability is significantly improved by the addition of triethylamine.[42] The same is true for the MX coordinated species; thus, crystal growth, spectroscopic measurements, and quantum yield measurements were performed in the presence of 1% triethylamine. Lastly, the coordination of MX into the alkyne tweezers significantly improves photostability (vide infra).

Structural Characterization. Crystal structures of **DMA·CuBr**, **TPA·CuBr**, **Ph·CuBr**, **Ph·CuCl**, and **Ph·AgCl** are reported herein (Figure 3, Table 1, Table S1, Figures S10−S14). This provides a complete set of CuBr coordinated into all three parent complexes as well as the complete set of $Cp_2Ti(C_2Ph)_2$ with all three MX. A variety of aryl ring rotations are observed for the alkynyl ligands of the various complexes, likely driven by packing interactions in the different structure types.

Coordination of MX into the alkyne tweezers of the titanocenes results in structural distortions consistent with other heterobimetallic tweezer molecules.[61,62] For example, the bond angles around the sp-hybridized carbons for the parent $Cp_2Ti(C_2Ph)_2$ and $Cp_2Ti(C_2DMA)_2$ are slightly distorted from 180° (172−179°), and the coordination of CuX into the complexes further distorts these Ti−C≡C and C≡C−C bond angles (164−169°, Table 1). The coordination of AgCl has less of an impact on these bond angles than CuX, that is, the sp hybridized bond angles in **Ph·AgCl** (171−172°) are closer to those of the parent. The coordination of MX also elongates the C≡C bond by 0.01 to 0.02 Å (Table 1). Lastly, the coordination of CuX compresses the C−Ti−C bond angle to a greater extent than the coordination of AgCl (Table 1). This is likely due to less compression being necessary to bond the alkynes to Ag^{I} than to Cu^{I}, due to their relative ionic radii.[65]

Along with these structural effects, the coordination of MX results in a decrease in ν(C≡C) relative to the parent complexes, with the coordination of CuX resulting in a greater decrease than the coordination of AgCl. Chiefly, the C≡C

https://doi.org/10.1021/acs.inorgchem.2c01746
Inorg. Chem. 2022, 61, 10986−10998

stretch for CuX complexes is 6 to 40 cm^{-1} lower in energy than the corresponding AgCl complexes (Figure S15). Both the structural and spectroscopic trends are consistent with Cu^I and Ag^I undergoing η^2-coordination of the alkynes to the metal.[61,66] As has been observed previously in Ag^I and Cu^I η^2-alkynyl complexes, the C≡C bond length is not as sensitive to the strength of the metal−alkynyl interaction as is the distortion of the angle about the sp-hybridized carbons or ν(C≡C).[66] Here, the larger decrease in ν(C≡C) and larger angular distortion about the sp-hybridized carbons upon CuX coordination compared with AgCl coordination indicates a stronger M−alkyne interaction for CuX. This is consistent with previously reported examples of Cu^I and Ag^I η^2-alkynyl complexes where Cu^I coordination impacts the structure to a greater extent.[61,66] In those cases, the spectroscopic, structural, and computational data suggest that the metal−alkynyl orbital interactions are dominated by alkynyl to M^I σ-donation rather than M^I to alkynyl π-backbonding.[66,67]

Photophysics. Each of the parent complexes has a low-energy absorbance band that has been ascribed to an LMCT transition.[42] The solution UV−vis spectrum of each MX coordinated complex has a similar low-energy absorption that is modestly red-shifted relative to the parent complexes in all cases except for **Ph·AgCl** (Figure 4). The coordination of CuX decreases the molar absorptivity to a greater extent than the coordination of AgCl, whereas the identity of the halide on Cu has little impact on either energy or molar absorptivity.

Upon excitation into the lowest-energy absorbance band, all complexes are brightly emissive in 2-methyltetrahydrofuran (2-MeTHF) glass at 77 K (Figure 5, Table 2) and weakly emissive at room temperature as a microcrystalline solid (Figure S16). The excitation spectra coincide with the main features in the corresponding absorption spectra, indicating that the emission is not due to an impurity (Figures S17−S20). In addition, both the $Cp_2Ti(C_2Ph)_2$ parent complex and the corresponding **Ph·AgCl** are weakly emissive in room-temperature air-saturated solution (Figure 5). For $Cp_2Ti(C_2Ph)_2$, $\Phi_{PL} \cong 2 \times 10^{-4}$ is unaffected by purging with argon. The emission of **Ph·AgCl** is approximately three times weaker. In solution, these complexes have nearly the same emission maximum as in 77 K glass, but with a broader high-energy tail, consistent with transitions from higher-energy vibronic states at RT. Its lifetime in RT solution is below the detection limit (200 ns) of our system. To our knowledge, this is the first report of emission in RT fluid solution for a Ti^{IV} complex.

Table 2. Experimental Emission Wavelengths and Lifetimes (77 K) and TDDFT and ΔSCF Calculated Lowest-Energy Triplet Transitions[a]

	exp[b]	TD-DFT[c]	ΔSCF[d]	lifetime[e]
$Cp_2Ti(C_2Ph)_2$	575[f]	569[f]	607	9.5 ms[g]
$Cp_2Ti(C_2TPA)_2$	642[f]	641[f]	727	9.6 ms[g]
$Cp_2Ti(C_2DMA)_2$	672[f]	670[f]	742	7.4 ms[g]
Ph·AgCl	578	573	610	1.1 ms
TPA·AgCl	659	685	790	20.2 us, 11 μs[h]
DMA·AgCl	723	718	801	35.7 us, 7.5 μs[h]
Ph·CuCl	706	558	655	19.8 μs
TPA·CuCl	708	677	816	31.2 μs
DMA·CuCl	748	720	848	28.5 μs
Ph·CuBr	715	562	668	19.4 μs
TPA·CuBr	700	673	810	45 μs
DMA·CuBr	767	722	857	41.5 μs

[a]See Figure 2 for complex abbreviations. [b]Exp is the experimentally determined emission maximum (2-MeTHF, 77 K), λ_{ex} = 400 nm. [c]The S_0 to T_1 transition was predicted using MN15/LANL2DZ//B3LYP/6-311+G(d)/DGDZVP. [d]Energy difference between B3LYP/6-311+G(d)/DGDZVP singlet optimization and single point triplet energy of the same geometry (T_1@S_0 − S_0@S_0). [e]Excited-state lifetime measured at the emission maximum (2-MeTHF, 77 K), λ_{ex} = 367 nm. [f]From ref 42. [g]There is a significantly shorter lifetime component that is not a major contributor to the integrated emission intensity (Figure S21). [h]Biexponential.

At 77 K, the coordination of MX results in a red-shift in the emission spectra relative to the corresponding parent for all complexes except **Ph·AgCl** (Figure 5). Coordination of CuX always resulted in a greater red-shift than coordination of AgCl, whereas the identity of the halide on Cu had less impact on the emission energy. The larger impact of CuX than AgCl on the emission spectra parallels the structural conclusions that there is a stronger M−alkyne interaction for CuX than for AgCl.

The coordination of MX into the parent complexes also decreases the excited-state lifetime (77 K) by nearly three orders of magnitude (Table 2), that is, from tens of milliseconds to tens of microseconds, likely due to increased spin−orbit coupling from the added CuX and AgCl.[68] One minor exception to this trend is that coordination of AgCl into $Cp_2Ti(C_2Ph)_2$ lowers the lifetime by only one order of magnitude. This is consistent with AgCl also having minimal impact on the absorption and emission spectra, suggesting less involvement of AgCl in the excited state. To further assess how MX coordination affects the orbital character of the excited states, computational modeling was performed.

Computational Modeling. *Computational Benchmarking.* Previously reported computational benchmarking on the $Cp_2Ti(C_2R)_2$ parent complexes demonstrated that the 77 K emission spectra and room-temperature absorption spectra were most accurately modeled using MN15/LANL2DZ for both geometry optimization and TD-DFT.[42] The MX coordinated complexes were investigated using this model and other models that performed well with the $Cp_2Ti(C_2R)_2$ parent complexes.[41,42] Initially, the structure of **DMA·CuBr** and **TPA·CuBr** were optimized using a range of computational models. Each of the optimized structures was used as input for TD-DFT using MN15/LANL2DZ to determine which model gave the best agreement with spectroscopic data. While ωB97XD/6-311+G(d) most accurately modeled the crystal structure for **DMA·CuBr** (Table S2), the MN15/LANL2DZ TD-DFT calculations using the B3LYP/6-311+G(d) geometries resulted in $S_0 \rightarrow S_1$ and $S_0 \rightarrow T_1$ transitions that most closely matched the experimental absorption and emission spectra, respectively (Table S3).

Next, pairing the B3LYP/6-311+G(d) optimized geometries with a range of TD-DFT models demonstrated that MN15/LANL2DZ//B3LYP/6-311+G(d) (denoted as TDDFT//OPT) gave the best agreement with the experimental absorption and emission spectra (Table S4). All AgCl-coordinated complexes were optimized using B3LYP/6-311+G(d) with the DGDZVP basis set for the silver. Lastly, because all spectroscopic data reported herein are recorded in THF or 2-MeTHF, all calculations employ a Tomasi polarizable continuum model (PCM) with the dielectric constant for THF.[69] It is worth mentioning that previous benchmarking investigation for the parent complexes demonstrated that the MN15/LANL2DZ//B3LYP/6-311+G(d)

https://doi.org/10.1021/acs.inorgchem.2c01746
Inorg. Chem. 2022, 61, 10986−10998

Table 3. TD-DFT and Population Analysis for Lowest-Energy Singlets[a]

	singlet		population analysis				
	exp[b]	TD-DFT[c]	Ti	Cp	C_2Ar	M	X
$Cp_2Ti(C_2Ph)_2$	417[d]	426[d]	4 → 68(64)	14 → 9(−5)	75 → 23(−52)		
$Cp_2Ti(C_2TPA)_2$	525[d]	534[d]	1 → 62(61)	6 → 8(2)	93 → 30(−63)		
$Cp_2Ti(C_2DMA)_2$	540[d]	542[d]	0 → 58(58)	3 → 9(6)	96 → 33(−63)		
Ph·AgCl	413	465	0 → 59(59)	7 → 7(0)	72 → 31(−41)	10 → 0(−10)	11 → 3(−8)
TPA·AgCl	547	568	0 → 56(56)	1 → 7(6)	93 → 34(−59)	3 → 3(0)	2 → 0(−2)
DMA·AgCl	581	573	0 → 56(56)	2 → 7(5)	94 → 34(−60)	4 → 3(−1)	1 → 0(−1)
Ph·CuCl	486	470	2 → 58(56)	11 → 7(−4)	59 → 28(−31)	13 → 5(−8)	15 → 1(−14)
TPA·CuCl	544	571	0 → 55(55)	1 → 6(5)	90 → 33(−57)	5 → 5(0)	4 → 1(−3)
DMA·CuCl	571	582	0 → 54(54)	1 → 6(5)	88 → 34(−54)	6 → 5(−1)	4 → 1(−3)
Ph·CuBr	492	479	2 → 58(56)	11 → 7(-4)	40 → 29(−14)	14 → 5(−9)	30 → 1(−29)
TPA·CuBr	550	569	0 → 55(55)	1 → 6(5)	89 → 33(−56)	4 → 5(1)	6 → 1(−5)
DMA·CuBr	571	583	0 → 54(54)	1 → 6(5)	88 → 34(−54)	6 → 5(−1)	5 → 1(−4)

[a]See Figure 2 for complex abbreviations. [b]Exp is the lowest-energy absorption maximum at 20 °C in THF. [c]Performed with MN15/LANL2DZ//B3LYP/6-311+G(d)/DGDZVP. [d]From ref 42.

model was nearly as reliable as MN15/LANL2DZ//MN15/LANL2DZ.[42]

Singlet Excited-State Orbital Character. The MN15/LANL2DZ/PCM//B3LYP/6-311+G(d)/PCM model reasonably predicts the lowest-energy singlet transition energies and the relative energy ordering compared to the absorption data (Table 3), but overestimates the oscillator strength relative to the higher-energy transitions (Figures S22−S24). For each complex, the lowest-energy singlet transition is primarily a highest occupied molecular orbital (HOMO) to the lowest unoccupied molecular orbital (LUMO) transition (Figures 6 and S25, S26). The HOMO is dominated by the arylalkynyl ligand, with some electron density on MX, and the LUMO is dominated by Ti^{IV}. For **Ph·MX**, the HOMO has more electron density on MX than for **TPA·MX** or **DMA·MX**. This suggests that the lowest-energy visible absorption for **Ph·MX** involves a ^{1}LMCT with some MX character. The lowest-energy singlet transition for **Ph·AgCl** and **Ph·CuCl** is primarily C_2Ar-to-Ti LMCT (Ar = aryl) but with significant MX-to-Ti MXMCT, whereas the lowest-energy singlet transition for **Ph·CuBr** is dominated by CuBr-to-Ti MXMCT with notable C_2Ar-to-Ti LMCT. This is demonstrated graphically by electron density difference maps (EDDMs) (Figures 6, S25, S26) and by the Mulliken population analysis (Table 3). For **TPA·MX** and **DMA·MX**, the population analysis shows the lowest-energy singlet transition to be dominated by C_2Ar-to-Ti LMCT with only a minor orbital character from MX. In all cases, the degree of MX-to-Ti CT increases in the order AgCl < CuCl < CuBr. This is in agreement with the electronegativity of Br vs Cl and the relative thermodynamic difficulty of Ag^I oxidation.[70] Furthermore, the degree of LMCT character increases in the order **Ph·MX** < **DMA·MX** ≅ **TPA·MX**, in agreement with the arylamine substituents being more electron-rich than phenyl.

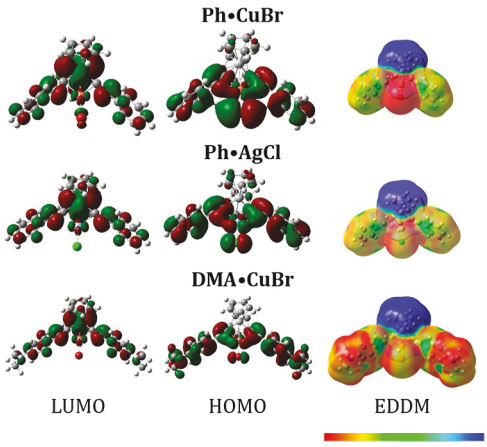

Figure 6. HOMO and LUMO for **Ph·CuBr**, **Ph·AgCl**, and **DMA·CuBr**. (isovalue of MO = 0.02 and density = 0.0004). Electron density difference maps (EDDM) based on TDDFT $S_0 \rightarrow S_1$ transition prepared with isovalue of MO = 0.02, density = 0.0002, and isovalue range = -7×10^{-6} to 7×10^{-6}. Red indicates a decrease in electron density and blue indicates an increase in electron density.

Triplet-Excited-State Orbital Character. TDDFT-determined S_0-to-T_1 transitions are often used to estimate observed emission bands in rigid matrices at 77 K due to a lack of structural rearrangement under such conditions.[71,72] The TDDFT-calculated lowest-energy triplets using the MN15/LANL2DZ//B3LYP/6-311+G(d) model are in poor agreement with the energy ordering of the emission spectra for both the **Ph·MX** complexes and the **TPA·MX** complexes (Table 2). Because of well-known issues with TDDFT calculations of triplet energies, ΔSCF methods are often preferred.[73,74] Given the lack of structural rearrangement likely in 77 K glass, ΔSCF calculations use the S_0 geometry. The S_0-to-T_1 transition energies predicted by ΔSCF calculations ($T_1@S_0 - S_0@S_0$) correctly predict the energy ordering between the complexes coordinated with different MX (Table 2), albeit while underpredicting the energies of all transitions with the exception of **Ph·CuX**.

Perhaps unsurprisingly, the calculated lowest-energy triplet reveals the same excited-state character as the S_0-to-S_1 transition, as demonstrated by Mulliken spin analysis of the triplet state, $T_1@S_0$ (Table S5). For example, the majority of the spin density is on the central titanium and the C_2Ar ligand, with a smaller density on coordinated MX. The MX spin density is larger for the **Ph·MX** complexes than the corresponding **DMA·MX** or **TPA·MX** complexes. The population analysis of the TDDFT transitions (Table S6) is also in agreement. Thus, the lowest-energy singlet and triplet transitions for **TPA·MX** and **DMA·MX** are suggested to be largely LMCT, while the corresponding transitions for **Ph·MX** are of mixed LMCT/MXMCT character with the MXMCT character dominating for **Ph·CuBr**.

https://doi.org/10.1021/acs.inorgchem.2c01746
Inorg. Chem. 2022, 61, 10986−10998

Table 4. Quantum Yields for Photodecomposition in RT Solution[a]

	parent[b]	AgCl	CuBr	CuCl
$Cp_2Ti(C_2Ph)_2$	0.99 (0.65)[c]	1.19 (1.52)[c]	1.5×10^{-2} (1.2×10^{-3})[c]	1.1×10^{-2} (1.2×10^{-3})[c]
$Cp_2Ti(C_2TPA)_2$	0.40	0.031	1.2×10^{-3}	7.3×10^{-4}
$Cp_2Ti(C_2DMA)_2$	0.25	4.5×10^{-3}	1.2×10^{-4}	1.8×10^{-4}

[a]**Ph·AgCl** was irradiated at 413 nm using a focused beam. The remaining MX coordinated complexes were irradiated using the Rayonet Photoreactor with 419 nm bulbs for **Ph·MX** and 575 nm bulbs for **DMA·MX** and **TPA·MX**. [b]From ref 42. [c]Quantum yields were determined in THF at room temperature under ambient air and under an Ar atmosphere (in parentheses). Only the complexes of $Cp_2Ti(C_2Ph)_2$ were sensitive to the presence of oxygen.

Impact of MX Coordination on Photostability. The parent $Cp_2Ti(C_2R)_2$ complexes photodecompose in RT solution with quantum yields between 0.25 and 0.99.[42] The coordination of MX into these titanocenes increases their photostability by one to three orders of magnitude (Table 4). The one exception is **Ph·AgCl**. This was also the only complex for which MX coordination did not impact the absorption and emission spectra. For this case, the coordination of AgCl actually *increases* the quantum yield for photodecomposition, Φ_{rxn}, to values larger than 1, which could be explained by secondary decompositions from photolysis of the AgCl photoproduct. Lastly, except for the complexes of $Cp_2Ti(C_2Ph)_2$, Φ_{rxn} is not sensitive to the presence of oxygen.

For the parent $Cp_2Ti(C_2R)_2$ complexes, the organic photoproduct is an enyne (**4** in Figure 7). Previous

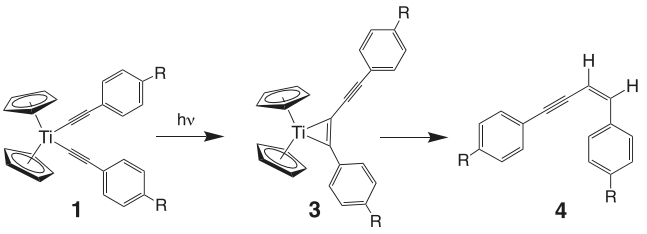

Figure 7. Photodecomposition scheme for $Cp_2Ti(C_2Ar)_2$.

investigations suggest **4** forms from reductive elimination of the two alkynyl ligands to give a butadiyne, followed by reduction of one of the alkynes to an alkene by the resulting "titanocene".[42,64] Furthermore, butadiynes are known to coordinate to titanocene to give metallacyclopropenes; and **3** (Figure 7), as well as its titanacyclocumulene form, has been suggested as a likely intermediate for photodecomposition.[75−77] The organic photoproducts for **Ph·CuBr** have been determined and mirror those of the corresponding parent complex (Figure S27), demonstrating that coordination of MX does not significantly impact the products of the reaction.

One notable trend regarding photostability is that Φ_{rxn} increases as the energy of the emissive state increases, and there appears to be a linear relationship between $\ln(\Phi_{rxn})$ and the energy of the emissive ^{3}CT state (Figure 8). One hypothesis for this observed correlation is that both emission and decomposition occur from the same ^{3}CT excited state and that the transition state for decomposition becomes increasingly thermally accessible as the ^{3}CT state energy increases, thereby increasing Φ_{rxn} (Figure 9). A similar correlation has been used as evidence for thermal access of an ^{3}MC state for a series of emissive platinum complexes.[78] Below we show that this hypothesis is consistent with the linear relationship shown in Figure 8.

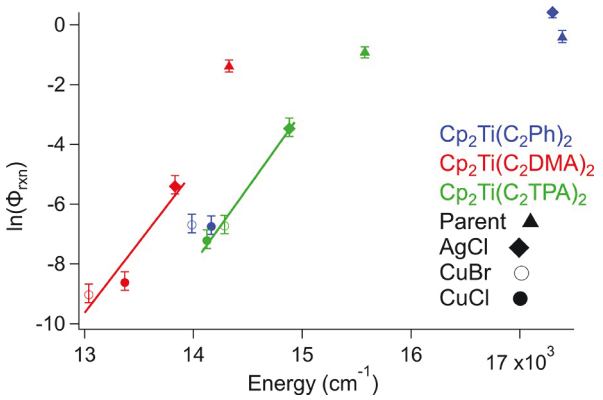

Figure 8. Plot of $\ln(\Phi_{rxn})$ vs emission energy. Only complexes with $\Phi_{rxn} < 0.1$ are included in the lines of best fit for **DMA·MX** (red) and **TPA·MX** (green).

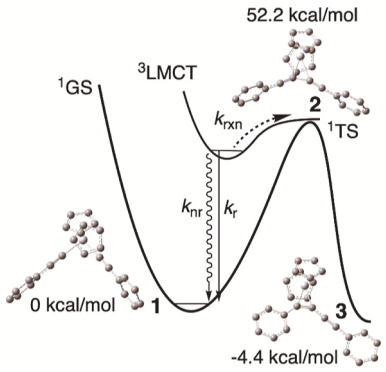

Figure 9. Gibbs free energy well for ground state (^{1}GS) $Cp_2Ti(C_2Ph)_2$ and calculated transition state (^{1}TS, **2**) for decomposition to a metallacyclopropene intermediate, **3**. The ^{3}LMCT excited-state potential well is displaced along the reaction coordinate.

First, an estimate of the Gibbs free energy of the transition state for decomposition requires the hypothesis of an initial reaction trajectory. Previous research suggests the formation of an intermediate metallocyclopropene (**3** in Figures 7 and 9).[77] Optimization of such an intermediate in THF solvent for the decomposition of $Cp_2Ti(C_2Ph)_2$ demonstrates it has a DLPNO-CCSD(T)/CBS/THF//ωB97X-D/6-311+G(d)/THF free energy of −4.4 kcal/mol relative to the starting titanocene, **1**. This structure was also found as a minimum by starting with an optimized Cp_2Ti fragment and 1,4-diphenylbutadiyne. A nudged elastic band transition-state (TS) calculation (also in THF) connecting **1** with **3** found a free-energy maximum at 52.2 kcal/mol (**2** in Figure 9), slightly higher than the emission energy of $Cp_2Ti(C_2Ph)_2$ (575 nm, 49.7 kcal/mol). An intrinsic reaction coordinate calculation confirmed that TS **2** does connect **1** to **3**. This suggests that

https://doi.org/10.1021/acs.inorgchem.2c01746
Inorg. Chem. 2022, 61, 10986−10998

the energy of the ^{3}CT excited state, E_{CT}, is lower than the energy of the transition state for ground-state decomposition, E_{TS}. This is in agreement with the hypothesis that intersystem crossing to the ground-state reaction surface is a thermally activated process (Figure 9). It is also interesting that the optimized ^{3}CT excited states of the $Cp_2Ti(C_2R)_2$ parent complexes are distorted along this reaction coordinate (i.e., elongated Ti−C bonds and a concomitant shortening of the distance between the carbon atoms attached to Ti).[42] Such a triplet distortion may lead to the critical geometry necessary to "jump" between surfaces.[79]

Further investigation of this mechanism requires representing Φ_{rxn} as a ratio of rate constants (eq 1).

$$\Phi_{rxn} = \frac{k_{rxn}}{k_r + k_{nr} + k_{rxn}}\Phi_{ISC} \cong \frac{k_{rxn}}{k_{nr} + k_{rxn}} \quad (1)$$

where k_{rxn} is the rate constant for the decomposition reaction, k_r is the radiative rate constant, and k_{nr} is the nonradiative rate constant—all from the ^{3}CT state; and Φ_{ISC} is the quantum yield for the formation of the ^{3}CT state from the initially formed singlet state. Approximating $\Phi_{ISC} \cong 1$ (by application of Ermolaev's rule; i.e., $\Phi_F + \Phi_{ISC} \cong 1$, where Φ_F is the fluorescence quantum yield),[79−81] Φ_{rxn} is controlled by competition between k_{rxn} and k_{nr} (given that k_r is negligible for these complexes at room temperature). When the quantum yield of decomposition is less than 0.1, then $k_{rxn} \ll k_{nr}$, resulting in eq 2.

$$\Phi_{rxn} \cong \frac{k_{rxn}}{k_{nr}} \therefore \ln(\Phi_{rxn}) \cong \ln(k_{rxn}) - \ln(k_{nr}) \quad (2)$$

Replacing k_{rxn} with an Arrhenius term (where the activation barrier is the energy difference between the transition state and the ^{3}CT state, $E_{TS}-E_{CT}$) and replacing k_{nr} with the expression for the energy-gap law[82] results in a linear dependence between $\ln(\Phi_{rxn})$ and the energy of the ^{3}CT state, E_{CT} (eq 3),

$$\ln(\Phi_{rxn}) \cong \text{const} + E_{CT}\left(\frac{1}{k_B T} + \frac{\gamma}{\hbar\omega}\right) \quad (3)$$

where the first term in the slope ($1/k_BT$, where k_B is the Boltzmann constant) comes from the Arrhenius term and the second term ($\gamma/\hbar\omega$, where ω is the maximum and dominant vibrational frequency available and γ is expressed in terms of more detailed molecular parameters) originates from the energy gap law.[82] Details of the derivation are presented in the Supporting Information.

According to this model, a plot of $\ln(\Phi_{rxn})$ *vs* E_{CT} should give a straight line with a slope of $\frac{1}{k_BT} + \frac{\gamma}{\hbar\omega}$ as long as eq 2 is valid, that is, when $\Phi_{rxn} < 0.1$. Such a linear relationship appears to be observed at low quantum yields (Figure 8). Furthermore, as k_{rxn} approaches k_{nr}, eq 2 is no longer valid, and eventually, Φ_{rxn} should asymptotically approach unity (and ln Φ_{rxn} approach 0) when $k_{rxn} \gg k_{nr}$. This is qualitatively observed (Figure 8). The slopes obtained for **DMA·MX** ($4.7 \pm 1.6 \times 10^{-3}$/cm^{-1}, Figure 8, red line) and **TPA·MX** ($5.1 \pm 0.4 \times 10^{-3}$/cm^{-1}, Figure 8, green line) are similar to the value of $1/k_BT$, which at room temperature is 4.8×10^{-3}/cm^{-1}. This suggests that $\gamma/\hbar\omega$ is relatively small compared to $1/k_BT$, which is consistent with some of the lower values for $\gamma/\hbar\omega$ determined from energy-gap-law plots for a range of systems (5×10^{-4} to 3.5×10^{-3}/cm^{-1}, Table S7).[83−89] No further conclusions regarding the magnitude of $\gamma/\hbar\omega$ can be made due to the limited size of the data set (and resulting uncertainty in the slope).

One assumption implicit in the abovementioned derivation is that E_{TS} is at higher energy than the ^{3}CT state and does not change significantly within each series of MX complexes (note that the parent complexes were not included in the calculations of the slope because $\Phi_{rxn} > 0.1$, and eqs 2 and 3 are not valid). The only complex for which E_{TS} was calculated is $Cp_2Ti(C_2Ph)_2$, the complex with the highest ^{3}CT-state energy. The addition of MX should only serve to increase the TS energy as MX will have to be expelled during the course of the reaction. Whether MX is still intimately connected to the TS is unknown. One *seeming* inconsistency in the data is that the value of Φ_{rxn} for **Ph·CuCl** and **Ph·CuBr** (Figure 8, blue circles) does not increase with increasing emission energy. This may be due to the fact that the identity of the excited state changes from being dominated by MXMCT for **Ph·CuBr** to LMCT for **Ph·CuCl** (vide supra). Recall that the excited states of all other MX coordinated complexes are dominated by LMCT.

The dependence of $\ln(\Phi_{rxn})$ on the ^{3}CT-state energy is consistent with emission and decomposition occurring from the same ^{3}CT excited state. An alternative mechanism involves a reaction from the initially formed singlet state prior to ISC. Though we cannot dismiss this mechanism, we note that no obvious trend between Φ_{rxn} and the lowest-energy absorption band is observed (Figure S28).

CONCLUSIONS AND OUTLOOK

Arylalkynyl titanocenes are an interesting class of emissive complexes, where the ^{3}LMCT emission can easily be tuned by the aryl substituents. The lack of photostability hinders the development of this class of compounds as photocatalysts. Herein, we have demonstrated that coordination of MX in the alkyne cleft of the complex greatly enhances the stability, while also lowering the lowest-energy absorption and emission energies. For most of the MX coordinated complexes, the TDDFT data suggest that the lowest-energy excited state is still of the ^{3}LMCT character. Only in the case of **Ph·CuBr** was there a greater degree of MX-to-Ti CT than ligand-to-Ti CT. Interestingly, for the case of **Ph·AgCl**, there was no difference in the absorption and emission energy from those of the corresponding parent complex, nor was there any increase in photostability. This suggests that MX is not simply serving to stabilize the complex toward decomposition through a chelate effect but rather that there is a relationship between the quantum yield for decomposition and the excited-state energy. Indeed, as the energy of the excited state increases, the quantum yield for photodecomposition increases. This is consistent with photoreactivity being controlled by a competition between thermally activated ISC from the ^{3}CT state to the ^{1}TS state for decomposition and nonradiative decay.

Lastly, we note that the complexes with the highest-energy ^{3}LMCT, $Cp_2Ti(C_2Ph)_2$ and **Ph·AgCl**, are the only complexes that show emission in RT fluid solution, albeit with $\Phi_{em} \leq 2 \times 10^{-4}$. This suggests that k_r is at least somewhat competitive with k_{nr} for $Cp_2Ti(C_2Ph)_2$ and **Ph·AgCl**. Note that for $Cp_2Ti(C_2TPA)_2$ and $Cp_2Ti(C_2DMA)_2$, no emission in RT fluid solution is observed, despite those complexes being more photostable. This suggests that for these parent complexes that $k_{nr} \gg k_r$ and that the reason the higher energy $Cp_2Ti(C_2Ph)_2$ complex is emissive in solution may in part be due to the energy-gap law. Such results suggest that careful design of

https://doi.org/10.1021/acs.inorgchem.2c01746
Inorg. Chem. 2022, 61, 10986−10998

group 4 metallocenes may lead to photostable complexes with lifetimes sufficient to act as photocatalysts. Such strategies may involve inhibiting vibrational modes leading to nonradiative deactivation.

■ ASSOCIATED CONTENT

Supporting Information

The Supporting Information is available free of charge at https://pubs.acs.org/doi/10.1021/acs.inorgchem.2c01746.

^{1}H NMR and ^{13}C NMR spectra; crystallographic data for **DMA·CuBr**, **TPA·CuBr**, **Ph·CuBr**, **Ph·CuCl**, and **Ph·AgCl**; several different orientations and packing arrangements for the solid-state structures; FTIR spectra of the C≡C stretching region; excitation and solid-state emission spectra; luminescence decay plots for $Cp_2Ti(C_2Ph)_2$, $Cp_2Ti(C_2TPA)_2$, and $Cp_2Ti(C_2DMA)_2$; comparison of the solid-state structure of **DMA·CuBr** with the optimized structure using several DFT models; comparison of emission and absorption data with predictions from several TDDFT models; HOMO/LUMO images and orbital contribution for $S_0 \rightarrow S_1$ and $S_0 \rightarrow T_1$ transitions; EDDMs based on TDDFT $S_0 \rightarrow S_1$ transitions; $S_0 \rightarrow T_1$ population analysis; Mulliken spin distribution for $T_1@S_0$, ^{1}H NMR spectrum of decomposition products for **Ph·CuBr**; and plot of $\ln(\Phi_{rxn})$ *versus* the energy of the lowest-energy absorption (PDF)

Cartesian coordinates for all singlet-optimized structures using B3LYP/6-311+G(d)/DGDZVP (XYZ)

Accession Codes

CCDC 2172550−2172554 contain the supplementary crystallographic data for this paper. These data can be obtained free of charge via www.ccdc.cam.ac.uk/data_request/cif, or by emailing data_request@ccdc.cam.ac.uk, or by contacting The Cambridge Crystallographic Data Centre, 12 Union Road, Cambridge CB2 1EZ, UK; fax: +44 1223 336033.

■ AUTHOR INFORMATION

Corresponding Authors

George C. Shields − *Department of Chemistry, Furman University, Greenville, South Carolina 29609, United States;* orcid.org/0000-0003-1287-8585; Email: george.sheilds@furman.edu

Paul S. Wagenknecht − *Department of Chemistry, Furman University, Greenville, South Carolina 29609, United States;* orcid.org/0000-0001-8698-073X; Email: paul.wagenknecht@furman.edu

Authors

Henry C. London − *Department of Chemistry, Furman University, Greenville, South Carolina 29609, United States*

David Y. Pritchett − *Department of Chemistry, Furman University, Greenville, South Carolina 29609, United States*

Jared A. Pienkos − *Department of Chemistry, Furman University, Greenville, South Carolina 29609, United States*

Colin D. McMillen − *Department of Chemistry, Clemson University, Clemson, South Carolina 29634, United States;* orcid.org/0000-0002-7773-8797

Thomas J. Whittemore − *Department of Chemistry, Furman University, Greenville, South Carolina 29609, United States*

Conor J. Bready − *Department of Chemistry, Furman University, Greenville, South Carolina 29609, United States*

Alexis R. Myers − *Department of Chemistry, Furman University, Greenville, South Carolina 29609, United States*

Noah C. Vieira − *Department of Chemistry, Furman University, Greenville, South Carolina 29609, United States*

Shannon Harold − *Department of Chemistry, Furman University, Greenville, South Carolina 29609, United States*

Complete contact information is available at: https://pubs.acs.org/10.1021/acs.inorgchem.2c01746

Notes

The authors declare no competing financial interest.

■ ACKNOWLEDGMENTS

This material is based upon work supported by the National Science Foundation under grant no. 2055326 and through the EPSCoR Program under NSF Award no. OIA-1655740. T.J.W. acknowledges summer support from NSF-REU (CHE-1757706). Any opinions, findings, conclusions, or recommendations expressed in this material are those of the authors and do not necessarily reflect those of the National Science Foundation. G.C.S. acknowledges a Research Corporation for Science Advancement Cottrell Instrumentation Supplements award #27446 and National Science Foundation grants CHE-1903871 and CHE-2018427. DYP acknowledges support from the Furman Summer Fellows Program. NCV acknowledges support through the Arnold and Mabel Beckman Foundation Beckman Scholars Award.

■ REFERENCES

(1) Twilton, J.; Le, C.; Zhang, P.; Shaw, M. H.; Evans, R. W.; MacMillan, D. W. C. The merger of transition metal and photocatalysis. *Nat. Rev. Chem* **2017**, *1*, 0052.

(2) Prier, C. K.; Rankic, D. A.; MacMillan, D. W. C. Visible Light Photoredox Catalysis with Transition Metal Complexes: Applications in Organic Synthesis. *Chem. Rev.* **2013**, *113*, 5322−5363.

(3) Idris, M.; Kapper, S. C.; Tadle, A. C.; Batagoda, T.; Muthiah Ravinson, D. S.; Abimbola, O.; Djurovich, P. I.; Kim, J.; Coburn, C.; Forrest, S. R.; Thompson, M. E. Blue Emissive fac/mer-Iridium (III) NHC Carbene Complexes and their Application in OLEDs. *Adv. Opt. Mater.* **2021**, *9*, 2001994.

(4) Gildea, L. F.; Williams, J. A. G. Iridium and platinum complexes for OLEDS. In *Woodhead Publishing Series in Electronic and Optical Materials, Organic Light-Emitting Diodes (OLEDs)*; Buckley, A., Ed.; Woodhead Publishing, 2013; pp 77−113.

(5) He, R.; Xu, Z.; Valandro, S.; Arman, H. D.; Xue, J.; Schanze, K. S. High-Purity and Saturated Deep-Blue Luminescence from trans-NHC Platinum(II) Butadiyne Complexes: Properties and Organic Light Emitting Diode Application. *ACS Appl. Mater. Interfaces* **2021**, *13*, 5327−5337.

(6) Law, A. S.-Y.; Lee, L. C.-C.; Lo, K. K.-W.; Yam, V. W.-W. Aggregation and Supramolecular Self-Assembly of Low-Energy Red Luminescent Alkynylplatinum(II) Complexes for RNA Detection, Nucleolus Imaging, and RNA Synthesis Inhibitor Screening. *J. Am. Chem. Soc.* **2021**, *143*, 5396−5405.

(7) Yip, A. M.-H.; Lai, C. K.-H.; Yiu, K. S.-M.; Lo, K. K.-W. Phosphorogenic Iridium(III) *bis*-Tetrazine Complexes for Bioorthogonal Peptide Stapling, Bioimaging, Photocytotoxic Applications, and the Construction of Nanosized Hydrogels. *Angew. Chem., Int. Ed.* **2022**, *61*, No. e202116078.

(8) Gowda, A. S.; Lee, T. S.; Rosko, M. C.; Petersen, J. L.; Castellano, F. N.; Milsmann, C. Long-Lived Photoluminescence of Molecular Group 14 Compounds through Thermally Activated Delayed Fluorescence. *Inorg. Chem.* **2022**, *61*, 7338−7348.

(9) Wenger, O. S. Photoactive Complexes with Earth-Abundant Metals. *J. Am. Chem. Soc.* **2018**, *140*, 13522−13533.

(10) Büldt, L. A.; Guo, X.; Prescimone, A.; Wenger, O. S. A Molybdenum(0) Isocyanide Analogue of Ru(2,2′-Bipyridine)$_3^{2+}$: A Strong Reductant for Photoredox Catalysis. *Angew. Chem., Int. Ed.* **2016**, *55*, 11247−11250.
(11) Sattler, W.; Henling, L. M.; Winkler, J. R.; Gray, H. B. Bespoke Photoreductants: Tungsten Arylisocyanides. *J. Am. Chem. Soc.* **2015**, *137*, 1198−1205.
(12) Sattler, W.; Ener, M. E.; Blakemore, J. D.; Rachford, A. A.; LaBeaume, P. J.; Thackeray, J. W.; Cameron, J. F.; Winkler, J. R.; Gray, H. B. Generation of Powerful Tungsten Reductants by Visible Light Excitation. *J. Am. Chem. Soc.* **2013**, *135*, 10614−10617.
(13) Wegeberg, C.; Wenger, O. S. Luminescent First-Row Transition Metal Complexes. *JACS Au* **2021**, *1*, 1860−1876.
(14) Glaser, F.; Wenger, O. S. Recent progress in the development of transition-metal based photoredox catalysts. *Coord. Chem. Rev.* **2020**, *405*, 213129.
(15) McCusker, J. K. Electronic structure in the transition metal block and its implications for light harvesting. *Science* **2019**, *363*, 484−488.
(16) Förster, C.; Heinze, K. Photophysics and Photochemistry with Earth-Abundant Metals − Fundamentals and Concepts. *Chem. Soc. Rev.* **2020**, *49*, 1057−1070.
(17) Wegeberg, C.; Wenger, O. S. Luminescent chromium(0) and manganese(I) complexes. *Dalton Trans.* **2022**, *51*, 1297−1302.
(18) Chábera, P.; Liu, Y.; Prakash, O.; Thyrhaug, E.; Nahhas, A. E.; Honarfar, A.; Essén, S.; Fredin, L. A.; Harlang, T. C. B.; Kjær, K. S.; Handrup, K.; Ericson, F.; Tatsuno, H.; Morgan, K.; Schnadt, J.; Häggström, L.; Ericsson, T.; Sobkowiak, A.; Lidin, S.; Huang, P.; Styring, S.; Uhlig, J.; Bendix, J.; Lomoth, R.; Sundström, V.; Persson, P.; Wärnmark, K. A low-spin Fe(III) complex with 100-ps ligand-to-metal charge transfer photoluminescence. *Nature* **2017**, *543*, 695−699.
(19) Otto, S.; Dorn, M.; Förster, C.; Bauer, M.; Seitz, M.; Heinze, K. Understanding and exploiting long-lived near-infrared emission of a molecular ruby. *Coord. Chem. Rev.* **2018**, *359*, 102−111.
(20) Kitzman, W. R.; Moll, J.; Heinze, K. Spin-flip luminescence. *Photochem. Photobiol. Sci* **2022**, DOI: 10.1007/s43630-022-00186-3.
(21) Wang, C.; Reichenauer, F.; Kitzmann, W. R.; Kerzig, C.; Heniz, K.; Resch-Genger, U. Efficient Triplet-Triplet Annihilation Upconversion Sensitized by a Cr(III) Complex via an Underexplored Energy Transfer Mechanism. *Angew. Chem., Int. Ed.* **2022**, No. e202202238.
(22) Armaroli, N.; Accorsi, G.; Cardinali, F.; Listorti, A. Photochemistry and Photophysics of Coordination Compounds: Copper. *Top. Curr. Chem.* **2007**, *280*, 69−115.
(23) Hsu, C.-W.; Lin, C.-C.; Chung, M.-W.; Chi, Y.; Lee, G.-H.; Chou, P.-T.; Chang, C.-H.; Chen, P.-Y. Systematic Investigation of the Metal-StructurePhotophysics Relationship of Emissive d^{10} Complexes of Group 11 Elements: The Prospect of Application in Organic Light Emitting Devices. *J. Am. Chem. Soc.* **2011**, *133*, 12085−12099.
(24) Liu, Y.; Yiu, S.-C.; Ho, C.-L.; Wong, W.-Y. Recent advances in copper complexes for electrical/light energy conversion. *Coord. Chem. Rev.* **2018**, *375*, 514−557.
(25) Brauchli, S. Y.; Malzner, F. J.; Constable, E. C.; Housecroft, C. E. Copper(i)-based dye-sensitized solar cells with sterically demanding anchoring ligands: bigger is not always better. *RSC Adv.* **2015**, *5*, 48516−48525.
(26) Rosko, M. C.; Wells, K. A.; Hauke, C. E.; Castellano, F. N. Next Generation Cuprous Phenanthroline MLCT Photosensitizer Featuring Cyclohexyl Substituents. *Inorg. Chem.* **2021**, *60*, 8394−8403.
(27) Ravetz, B. D.; Wang, J. Y.; Ruhl, K. E.; Rovis, T. Photoinduced Ligand-to-Metal Charge Transfer Enables Photocatalyst-Independent Light-Gated Activation of Co(II). *ACS Catal.* **2019**, *9*, 200−204.
(28) Shields, B. J.; Kudisch, B.; Scholes, G. D.; Doyle, A. G. Long-Lived Charge-Transfer States of Nickel(II) Aryl Halide Complexes Facilitate Bimolecular Photoinduced Electron Transfer. *J. Am. Chem. Soc.* **2018**, *140*, 3035−3039.
(29) Wagenknecht, P. S.; Ford, P. C. Metal Centered Ligand Field Excited States: Their Roles in the Design and Performance of Transition Metal Based Photochemical Molecular Devices. *Coord. Chem. Rev.* **2011**, *255*, 591−616.
(30) Zhang, Y.; Petersen, J. L.; Milsmann, C. A Luminescent Zirconium(IV) Complex as a Molecular Photosensitizer for Visible Light Photoredox Catalysis. *J. Am. Chem. Soc.* **2016**, *138*, 13115−13118.
(31) Zhang, Y.; Lee, T. S.; Favale, J. M.; Leary, D. C.; Petersen, J. L.; Scholes, G. D.; Castellano, F. N.; Milsmann, C. Delayed fluorescence from a zirconium(IV) photosensitizer with ligand-to-metal charge-transfer excited states. *Nat. Chem.* **2020**, *12*, 345−352.
(32) Yang, M.; Sheykhi, S.; Zhang, Y.; Milsmann, C.; Castellano, F. N. Low power threshold photochemical upconversion using a zirconium(IV) LMCT photosensitizer. *Chem. Sci.* **2021**, *12*, 9069−9077.
(33) Romain, C.; Choua, S.; Collin, J.-P.; Heinrich, M.; Bailly, C.; Karmazin-Brelot, L.; Bellemin-Laponnaz, S.; Dagorne, S. Redox and Luminescent Properties of Robust and Air-Stable N-Heterocyclic Carbene Group 4 Metal Complexes. *Inorg. Chem.* **2014**, *53*, 7371−7376.
(34) Pfennig, B. W.; Thompson, M. E.; Bocarsly, A. B. A New Class of Room Temperature Luminescent Organometallic Complexes: Luminescence and Photophysical Properties of Permethylscandocene Chloride in Fluid Solution. *J. Am. Chem. Soc.* **1989**, *111*, 8947−8948.
(35) Kenney, J. W.; Boone, D. R.; Striplin, D. R.; Chen, Y. H.; Hamar, K. B. Electronic luminescence spectra of charge transfer states of titanium(IV) metallocenes. *Organometallics* **1993**, *12*, 3671−3676.
(36) Patrick, E. L.; Ray, C. J.; Meyer, G. D.; Ortiz, T. P.; Marshall, J. A.; Brozik, J. A.; Summers, M. A.; Kenney, J. W. Non-Localized Ligand-to-Metal Charge Transfer Excited States in $(Cp)_2Ti(IV)(NCS)_2$. *J. Am. Chem. Soc.* **2003**, *125*, 5461−5470.
(37) Loukova, G. V.; Huhn, W.; Vasiliev, V. P.; Smirnov, V. A. Ligand-to-Metal Charge Transfer Excited States with Unprecedented Luminescence Yield in Fluid Solution. *J. Phys. Chem. A* **2007**, *111*, 4117−4121.
(38) Loukova, G. V.; Milov, A. A.; Vasiliev, V. P.; Minkin, V. I. Dipole moments and solvatochromism of metal complexes: principle photophysical and theoretical approach. *Phys. Chem. Chem. Phys.* **2016**, *18*, 17822−17826.
(39) Fermi, A.; Gualandi, A.; Bergamini, G.; Cozzi, P. G. Shining Light on Ti^{IV} Complexes: Exceptional Tools for Metallaphotoredox Catalysis. *Eur. J. Org. Chem.* **2020**, *2020*, 6955−6965.
(40) Zhang, Z.; Hilche, T.; Slak, D.; Rietdijk, N. R.; Oloyede, U. N.; Flowers, R. A., II; Gansäuer, A. Titanocenes as Photoredox Catalysts Using Green-Light Irradiation. *Angew. Chem., Int. Ed.* **2020**, *59*, 9355−9359.
(41) Pienkos, J. A.; Agakidou, A. D.; Trindle, C. O.; Herwald, D. W.; Altun, Z.; Wagenknecht, P. S. Titanocene as a New Acceptor (A) for Arylamine Donors (D) in D-π-A Chromophores. *Organometallics* **2016**, *35*, 2575−2578.
(42) London, H. C.; Whittemore, T. J.; Gale, A. G.; McMillen, C. D.; Pritchett, D. Y.; Myers, A. R.; Thomas, H. D.; Shields, G. C.; Wagenknecht, P. S. Ligand-to-Metal Charge-Transfer Photophysics and Photochemistry of Emissive d^0 Titanocenes: A Spectroscopic and Computational Investigation. *Inorg. Chem.* **2021**, *60*, 14399−14409.
(43) Vieira, N. C.; Pienkos, J. A.; McMillen, C. D.; Myers, A. R.; Clay, A. P.; Wagenknecht, P. S. A trans-bidentate bis-pyridinyl ligand with a transition metal hinge. *Dalton Trans.* **2017**, *46*, 15195−15199.
(44) Hatchard, C. G.; Parker, C. A. A New Sensitive Chemical Actinometer—II. Potassium Ferrioxalate as a Standard Chemical Actinometer. *Proc. R. Soc. London, Ser. A* **1956**, *235*, 518−536.
(45) Frisch, M. J.; Trucks, G. W.; Schlegel, H. B.; Scuseria, G. E.; Robb, M. A.; Cheeseman, J. R.; Scalmani, G.; Barone, V.; Petersson, G. A.; Nakatsuji, H.; Li, X.; Caricato, M.; Marenich, A. V.; Bloino, J.; Janesko, B. G.; Gomperts, R.; Mennucci, B.; Hratchian, H. P.; Ortiz, J. V.; Izmaylov, A. F.; Sonnenberg, J. L.; Williams-Young, D.; Ding, F.; Lipparini, F.; Egidi, F.; Goings, J.; Peng, B.; Petrone, A.; Henderson, T.; Ranasinghe, D.; Zakrzewski, V. G.; Gao, J.; Rega, N.; Zheng, G.; Liang, W.; Hada, M.; Ehara, M.; Toyota, K.; Fukuda, R.; Hasegawa, J.; Ishida, M.; Nakajima, T.; Honda, Y.; Kitao, O.; Nakai, H.; Vreven, T.;

Throssell, K.; Montgomery, J. A., Jr.; Peralta, J. E.; Ogliaro, F.; Bearpark, M. J.; Heyd, J. J.; Brothers, E. N.; Kudin, K. N.; Staroverov, V. N.; Keith, T. A.; Kobayashi, R.; Normand, J.; Raghavachari, K.; Rendell, A. P.; Burant, J. C.; Iyengar, S. S.; Tomasi, J.; Cossi, M.; Millam, J. M.; Klene, M.; Adamo, C.; Cammi, R.; Ochterski, J. W.; Martin, R. L.; Morokuma, K.; Farkas, O.; Foresman, J. B.; Fox, D. J. *Gaussian 16*; Revision C.01; Gaussian, Inc.: Wallingford CT, 2016.

(46) Dennington, R.; Keith, T. A.; Millam, J. M. *GaussView*; version 6; Semichem Inc.: Shawnee Mission, KS, 2016.

(47) O'Boyle, N. M.; Tenderholt, A. L.; Langner, K. M. cclib: A library for package-independent computational chemistry algorithms. *J. Comput. Chem.* **2008**, *29*, 839−845.

(48) (a) Becke, A. D. Density-functional exchange-energy approximation with correct asymptotic behavior. *Phys. Rev. A: At., Mol., Opt. Phys.* **1988**, *38*, 3098−3100. (b) Lee, C.; Yang, W.; Parr, R. G. Development of the Colle-Salvetti correlation-energy formula into a functional of the electron density. *Phys. Rev. B: Condens. Matter Mater. Phys.* **1988**, *37*, 785−789.

(49) Yu, H. S.; He, X.; Li, S. L.; Truhlar, D. G. MN15: A KohnSham global-hybrid exchange-correlation density functional with broad accuracy for multi-reference and single-reference systems and noncovalent interactions. *Chem. Sci.* **2016**, *7*, 5032−5051.

(50) Chai, J.-D.; Head-Gordon, M. Long-range corrected hybrid density functionals with damped atom-atom dispersion corrections. *Phys. Chem. Chem. Phys.* **2008**, *10*, 6615−6620.

(51) (a) McLean, A. D.; Chandler, G. S. Contracted Gaussian-basis sets for molecular calculations. 1. 2nd row atoms, Z = 11−18. *J. Chem. Phys.* **1980**, *72*, 5639−5648. (b) Wachters, A. J. H. Gaussian basis set for molecular wavefunctions containing third-row atoms. *J. Chem. Phys.* **1970**, *52*, 1033−1036. (c) Hay, P. J. Gaussian basis sets for molecular calculations-representation of 3D orbitals in transition-metal atoms. *J. Chem. Phys.* **1977**, *66*, 4377−4384. (d) Clark, T.; Chandrasekhar, J.; Spitznagel, G. n. W.; Schleyer, P. V. R. Efficient diffuse function-augmented basis-sets for anion calculations. 3. The 3-21+G basis set for 1st-row elements, Li-F. *J. Comput. Chem.* **1983**, *4*, 294−301. (e) Frisch, M. J.; Pople, J. A.; Binkley, J. S. Self-Consistent Molecular Orbital Methods. 25. Supplementary Functions for Gaussian Basis Sets. *J. Chem. Phys.* **1984**, *80*, 3265−3269.

(52) (a) Godbout, N.; Salahub, D. R.; Andzelm, J.; Wimmer, E. Optimization of Gaussian-Type Basis Sets for Local Spin Density Functional Calculations. Part I. Boron through Neon, Optimization Technique and Validation. *Can. J. Chem.* **1992**, *70*, 560−571. (b) Sosa, C.; Andzelm, J.; Elkin, B. C.; Wimmer, E.; Dobbs, K. D.; Dixon, D. A. A Local Density Functional Study of the Structure and Vibrational Frequencies of Molecular Transition-Metal Compounds. *J. Phys. Chem.* **1992**, *96*, 6630−6636.

(53) Dunning, T. H.; Hay, P. J. *Modern Theoretical Chemistry*; Schaefer, H. F., Ed.; Plenum: New York, 1977; Vol. 3, pp 1−28.

(54) Neese, F.; Wennmohs, F.; Becker, U.; Riplinger, C. The Orca Quantum Chemistry Program Package. *Chem. Phys.* **2020**, *152*, 224108.

(55) Riplinger, C.; Pinski, P.; Becker, U.; Valeev, E. F.; Neese, F. Sparse Maps—a Systematic Infrastructure for Reduced-Scaling Electronic Structure Methods. II. Linear Scaling Domain Based Pair Natural Orbital Coupled Cluster Theory. *Chem. Phys.* **2016**, *144*, 024109.

(56) Wilson, A. K.; van Mourik, T.; Dunning, T. H. Gaussian Basis Sets for Use in Correlated Molecular Calculations. Vi. Sextuple Zeta Correlation Consistent Basis Sets for Boron through Neon. *J. Mol. Struct.* **1996**, *388*, 339−349.

(57) Gale, A. G.; Odbadrakh, T. T.; Ball, B. T.; Shields, G. C. Water-Mediated Peptide Bond Formation in the Gas Phase: A Model Prebiotic Reaction. *J. Phys. Chem. A* **2020**, *124*, 4150−4159.

(58) Gale, A. G.; Odbadrakh, T. T.; Shields, G. C. Catalytic Activity of Water Molecules in Gas-Phase Glycine Dimerization. *Int. J. Quantum Chem.* **2020**, *120*, No. e26469.

(59) *APEX 3*; v2017.3; Bruker-AXS Inc.: Madison, WI, 2017.

(60) Sheldrick, G. M. Crystal structure refinement with SHELXL. *Acta Crystallogr., Sect. C: Struct. Chem.* **2015**, *71*, 3−8.

(61) Lang, H.; Köhler, K.; Rheinwald, G.; Zsolnai, L.; Büchner, M.; Driess, A.; Huttner, G.; Strähle, J. Monomeric Alkyne-Stabilized Complexes of Organo−Copper(I) and −Silver(I). *Organometallics* **1999**, *18*, 598−605.

(62) Janssen, M. D.; Herres, M.; Zsolnai, L.; Grove, D. M.; Spek, A. L.; Lang, H.; van Koten, G. A Stable Bimetallic Copper(I) Titanium Acetylide. *Organometallics* **1995**, *14*, 1098−1100.

(63) Pienkos, J. A.; Webster, A. B.; Piechota, E. J.; Agakidou, A. D.; McMillen, C. D.; Pritchett, D. Y.; Meyer, G. J.; Wagenknecht, P. S. Oxidatively Stable Ferrocenyl-π-Bridge-Titanocene D−π-a Complexes: An Electrochemical and Spectroscopic Investigation of the Mixed-Valent States. *Dalton Trans.* **2018**, *47*, 10953−10964.

(64) Turlington, M. D.; Pienkos, J. A.; Carlton, E. S.; Wroblewski, K. N.; Myers, A. R.; Trindle, C. O.; Altun, Z.; Rack, J. J.; Wagenknecht, P. S. Complexes with Tunable Intramolecular Ferrocene to Ti(IV) Electronic Transitions: Models for Solid State Fe(II) to Ti(IV) Charge Transfer. *Inorg. Chem.* **2016**, *55*, 2200−2211.

(65) Ahrens, L. H. The Use of Ionization Potentials Part 1. Ionic Radii of the Elements. *Geochim. Cosmochim. Acta* **1952**, *2*, 155−169.

(66) Dias, H. V. R.; Flores, J. A.; Wu, J.; Kroll, P. Monomeric Copper(I), Silver(I), and Gold(I) Alkyne Complexes and the Coinage Metal Family Group Trends. *J. Am. Chem. Soc.* **2009**, *131*, 11249−11255.

(67) Das, A.; Dash, C.; Celik, M. A.; Yousufuddin, M.; Frenking, G.; Dias, H. V. R. Tris(Alkyne) and Bis(Alkyne) Complexes of Coinage Metals: Synthesis and Characterization of $(Cyclooctyne)_3M^+$ (M = Cu, Ag) and $(Cyclooctyne)_2Au^+$ and Coinage Metal (M = Cu, Ag, Au) Family Group Trends. *Organometallics* **2013**, *32*, 3135−3144.

(68) McGlynn, S. P.; Reynolds, M. J.; Daigre, G. W.; Christodoyleas, N. D. The External Heavy-Atom Spin-Orbital Coupling Effect. III. Phosphorescence Spectra and Lifetimes of Externally Perturbed Naphthalenes. *J. Phys. Chem.* **1962**, *66*, 2499−2505.

(69) Tomasi, J.; Mennucci, B.; Cammi, R. Quantum Mechanical Continuum Solvation Models. *Chem. Rev.* **2005**, *105*, 2999−3094.

(70) Połczyński, P.; Jurczakowski, R.; Grochala, W. Stabilization and Strong Oxidizing Properties of Ag(II) in a Fluorine-Free Solvent. *Chem. Commun.* **2013**, *49*, 7480−7482.

(71) Morello, G. R. Accurate Prediction of Emission Energies with TD-DFT Methods for Platinum and Iridium OLED Materials. *J. Mol. Model.* **2017**, *23*, 174.

(72) Niehaus, T. A.; Hofbeck, T.; Yersin, H. Charge-Transfer Excited States in Phosphorescent Organo-Transition Metal Compounds: A Difficult Case for Time Dependent Density Functional Theory? *RSC Adv.* **2015**, *5*, 63318−63329.

(73) Sears, J. S.; Koerzdoerfer, T.; Zhang, C.-R.; Brédas, J.-L. Oribital instabilities and triplet states from time-dependent density functional theory and long-range corrected functionals. *J. Chem. Phys.* **2011**, *135*, 151103.

(74) Davies, D. L.; Lelj, F.; Lowe, M. P.; Ryder, K. S.; Singh, K.; Singh, S. Pyridine imines as ligands in luminescent iridum complexes. *Dalton Trans.* **2014**, *43*, 4026−4039.

(75) Pulst, S.; Arndt, P.; Heller, B.; Baumann, W.; Kempe, R.; Rosenthal, U. Nickel(0) Complexes of Five-Membered Titana- and Zirconacyclocumulenes as Intermediates in the Cleavage of C-C Bonds of Disubstituted Butadiynes. *Angew. Chem., Int. Ed. Engl.* **1996**, *35*, 1112−1115.

(76) Burlakov, V. V.; Peulecke, N.; Baumann, W.; Spannenberg, A.; Kempe, R.; Rosenthal, U. Reactions of the phenyl-substituted five-membered titanacyclocumulene a″ Unusual coupling of a 1,4-disubstituted 1,3-butadiyne with two titanium atoms. *J. Organomet. Chem.* **1997**, *536*−*537*, 293−297.

(77) Jemmis, E. D.; Phukan, A. K.; Giju, K. T. Dependence of the Structure and Stability of Cyclocumulenes and Cyclopropenes on the Replacement of the CH_2 Group by Titanocene and Zirconocene: A Density Functional Theory Study. *Organometallics* **2002**, *21*, 2254−2261.

(78) Bullock, J. D.; Valandro, S. R.; Sulicz, A. N.; Zeman, C. J.; Abboud, K. A.; Schanze, K. S. Blue Phosphorescent *Trans*-n-

https://doi.org/10.1021/acs.inorgchem.2c01746
Inorg. Chem. 2022, 61, 10986−10998

Heterocyclic Carbene Platinum Acetylides: Dependence on Energy Gap and Conformation. *J. Phys. Chem. A* **2019**, *123*, 9069−9078.
(79) Turro, N. J. *Modern Molecular Photochemistry*; University Science Books: Sausalito, California, 1991.
(80) Ermolaev, V. L.; Sveshnikova, E. B. Limits to the Applicability of the Rule of Equality to Unity of the Sum of Quantum Yields of Fluorescence and Transition to the Triplet State for Complex Organic Molecules in the Condensed Phase (a Review). *Opt. Spectrosc.* **2015**, *119*, 642−655.
(81) Ermolaev, V. L. Energy Transfer in Organic Systems Involving the Triplet State III. Rigid Solutions and Crystals. *Sov. Phys. Usp.* **1963**, *6*, 333−358.
(82) Englman, R.; Jortner, J. The Energy Gap Law for Non-Radiative Decay in Large Molecules. *J. Lumin.* **1970**, *1*−*2*, 134−142.
(83) Atallah, H.; Taliaferro, C. M.; Wells, K. A.; Castellano, F. N. Photophysics and Ultrafast Processes in Rhenium(I) Diimine Dicarbonyls. *Dalton Trans.* **2020**, *49*, 11565−11576.
(84) Caspar, J. V.; Kober, E. M.; Sullivan, B. P.; Meyer, T. J. Application of the Energy Gap Law to the Decay of Charge-Transfer Excited States. *J. Am. Chem. Soc.* **1982**, *104*, 630−632.
(85) Collado-Fregoso, E.; Pugliese, S. N.; Wojcik, M.; Benduhn, J.; Bar-Or, E.; Perdigón Toro, L.; Hörmann, U.; Spoltore, D.; Vandewal, K.; Hodgkiss, J. M.; Neher, D. Energy-Gap Law for Photocurrent Generation in Fullerene-Based Organic Solar Cells: The Case of Low-Donor-Content Blends. *J. Am. Chem. Soc.* **2019**, *141*, 2329−2341.
(86) Della Ciana, L.; Dressick, W. J.; Sandrini, D.; Maestri, M.; Ciano, M. Synthesis and Characterization of a New Family of Luminescent Cis-(4,4′-X_2-5,5′-Y_2-2,2′-Bipyridine)$_2$Os(CO)Cl(PF_6) Complexes (X = NEt_2, OMe, Me, H, Cl, Y = H; X = H, Y = Me; X = Y = Me): Control of Excited-State Properties by Bipyridyl Substituents. *Inorg. Chem.* **1990**, *29*, 2792−2798.
(87) Fajardo, J.; Schwan, J.; Kramer, W. W.; Takase, M. K.; Winkler, J. R.; Gray, H. B. Third-Generation W(CNAr)$_6$ Photoreductants (CNAr = Fused-Ring and Alkynyl-Bridged Arylisocyanides). *Inorg. Chem.* **2020**, *60*, 3481−3491.
(88) Lumpkin, R. S.; Meyer, T. J. Effect of the Glass-to-Fluid Transition on Excited-State Decay. Application of the Energy Gap Law. *J. Phys. Chem.* **1986**, *90*, 5307−5312.
(89) Wilson, J. S.; Chawdhury, N.; Al-Mandhary, M. R. A.; Younus, M.; Khan, M. S.; Raithby, P. R.; Köhler, A.; Friend, R. H. The Energy Gap Law for Triplet States in PT-Containing Conjugated Polymers and Monomers. *J. Am. Chem. Soc.* **2001**, *123*, 9412−9417.

https://doi.org/10.1021/acs.inorgchem.2c01746
Inorg. Chem. 2022, 61, 10986−10998